COMPUTATION OF CRACK PROPAGATION AND ARREST BY SIMULATING MICROFRACTURING AT THE CRACK TIP

EPRI NP-412
(Research Project 499)

Final Report

April 1977

Prepared by

Stanford Research Institute
333 Ravenswood Avenue
Menlo Park, California 94025

Principal Investigators
D. A. Shockey
L. Seaman
D. R. Curran

Prepared for

Electric Power Research Institute
3412 Hillview Avenue
Palo Alto, California 94304

Project Manager
Dr. Karl Stahlkopf

LEGAL NOTICE

FOREWORD

The ability to assess the safety and integrity of an engineering structure such as a nuclear reactor pressure vessel depends upon our ability to accurately describe what conditions are necessary to cause a crack to initiate from a flawed area. Once a crack has initiated, we must further know how to predict whether the crack will safely arrest or continue propagation and cause a structural failure.

Prevention of crack initiation is the first design defense against structural failure. The ASME Boiler and Pressure Vessel Code lays down conservative design procedures to prevent the initiation event from taking place. However, to further assure the continued safety and integrity of nuclear reactor pressure vessels, we must develop the analytical ability to assure that in the unlikely event of actual crack initiation, the crack will arrest rather than propagate. The traditional method of assessing the propagation-arrest event has been through the use of the fracture mechanics parameter, K_{Ia}, crack arrest toughness. However, this approach is presently clouded by controversy concerning whether K_{Ia} is actually a material property.

This report presents the results of a study to evaluate an alternate method of describing the crack propagation and arrest event. This new methodology models the nucleation, growth, and coolescence of microfractures ahead of a running crack and how these parameters effect the arrest event. It provides a link between physically observed micromechanical material behavior and the traditional fracture mechanics approach to the propagation and arrest event.

Karl Stahlkopf
Program Manager

ABSTRACT

A model that describes the nucleation, growth, and coalescence of microfractures under dynamic loading conditions was used in computational simulations of a DCB crack arrest experiment. The energy absorbed in plastic deformation and in microfracturing of material at the tip of a propagating crack was calculated, and the results agreed well with the fracture toughness calculations made by more conventional although more indirect methods. Agreement between computed and observed crack velocity and arrest length was not good, but should improve when a finer mesh is used. This approach provides a link between micromechanical material response and continuum toughness parameters.

ACKNOWLEDGEMENT

The stress wave calculations were performed by M. A. Austin.

CONTENTS

ILLUSTRATIONS

I INTRODUCTION AND SUMMARY

The design technology that emerged in the 1950s from linear elastic fracture mechanics (LEFM) concepts has enabled us to resolve a wide variety of crack initiation problems; however, research aimed at applying these concepts to problems of crack propagation and arrest has not given completely satisfactory results. For example, current attempts to develop a predictive capability for crack arrest by applying continuum fracture mechanics concepts have met with problems arising from kinetic effects in the process zone near the crack tip. Crosley and Ripling[1] indicated that the stress intensity factor at crack arrest, K_{Ia}, is a material property; Hahn and coworkers[2] suggested that the geometry-dependent kinetic energy associated with a running crack influences crack arrest and that, therefore, K_{Ia} cannot be a material property. This discrepancy demonstrates a need for an improved understanding of the nature of energy dissipation at the tip of a propagating crack.

This report describes the initial development stages of a computational capability for fast fracture and arrest, based on treatment of plastic flow and microfracturing in the material at the crack tip. The approach is to model the events occurring within the failing material traversed by the crack, compute the associated energies, and thereby determine the fracture toughnesses of propagating and arresting cracks. The fracture toughness is thus determined directly from the response of the material at the crack tip that actually deforms and fails as the crack propagates. This approach differs from usual methods of determining fracture toughness, in which elastic strain energy and kinetic energy are computed in the undeformed regions of the specimen and the difference taken to be the fracture toughness.

A Battelle DCB crack arrest experiment was computationally simulated by using a wave propagation code and the SRI nucleation and growth (NAG) fracture model. The TOODY3 wave propagation code, which as the ability to compute the transient stresses at the tip of the propagating crack, was adapted to the wedge-opening loaded double cantilever beam geometry. The method of dynamic relaxation was incorporated into the code to allow computation within an economical time of the static stress field at the point of instability. The computations allow for "bounce back" of the specimen from the base plate during crack propagation.

Fractographic examination of a broken DCB crack arrest specimen of 4340 steel gave results consistent with a crack propagation mechanism entailing nucleation, growth, and coalescence of microfractures at the crack tip. This mechanism was modeled computationally by incorporating into the wave propagation code as the fracture subroutine the laws found by SRI to describe rates of microfracture nucleation and growth in steels and other materials under stress wave loads. The microfracturing parameters for 4340 steel have never been measured; it was therefore necessary to use the measured parameters for a similar steel. Procedures for calculating and printing out the energies associated with microfracture activity and plastic flow were developed and incorporated.

The computed running crack toughness values agreed well with those obtained by continuum methods. The work absorbed in plastic deformation accounted for 95 percent of the total propagation energy, whereas the energy absorbed by microfracturing contributed only 5 percent to the toughness. However, the microfracturing process controls the extent of plastic work, and hence, the fracture toughness. Agreement between measured and computed crack velocity and arrest length was not satisfactory but could be improved by using a finer computational grid and

the actual dynamic fracture properties for the 4340 steel used in the Battelle specimen.

The program demonstrated the feasibility of using detailed and more physically realistic phenomenological models to solve fracture problems. This work appears to have been the first attempt to compute the behavior of a running and arresting crack by modeling nucleation, growth, and coalescence of microfracture in the failing material at the crack tip. The approach offers a way to link micromechanical material behavior to continuum toughness parameters.

II FRACTURE MECHANISMS AND MODELS

Substantial evidence indicates that crack propagation occurs by microfracture activity in the region slightly ahead of the crack front.[3] Figure 1 shows the partially failed material at the tip of a crack in Fe-3 Si steel. This photomicrograph was obtained by sectioning a double cantilever beam (DCB) specimen on a plane normal to the crack front. By removing successively thin layers of material from the sectioned surface, Hoagland et al.[4] determined that the microfractures were linked both with each other and with the crack front.

The inherent weak spots in material are responsible for this mechanism of crack propagation. Favorably oriented grain boundaries and cleavage planes are common weak spots. Inclusions and second-phase particles also initiate microfractures by either interfacial debonding or cracking of the particles themselves.[5,6] The weak spots in the path of the propagating crack can fail before the crack front arrives, because of the magnified stresses preceding the crack.

The details of this mechanism have not been quantitatively modeled. Crack propagation is usually treated as the movement through a homogeneous medium of a continuous crack front separating broken from unbroken material. This approach is computationally simple and often provides adequate results for design purposes. (For example, the toughness of a material with respect to crack initiation is a material property that is based on continuum considerations and has found considerable practical use.) In other instances, however, simplified continuum approaches have encountered difficulties, such as in describing crack arrest.

Large computers have to a large extent eliminated the need to make simplifying continuum assumptions to obtain a mathematical solution and have made possible more realistic treatments of crack propagation.

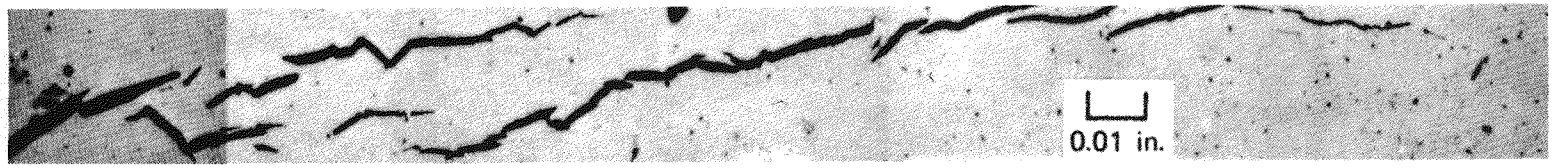

FIGURE 1 MICROCRACKS NEAR THE CRACK TIP OF A DOUBLE CANTILEVER BEAM SPECIMEN OF Fe-3 Si STEEL

Unfortunately, most researchers using large computers to solve fracture problems tend to concentrate on making better representations of geometries and put little additional sophistication into modeling the fracture process. As a result, our understanding of the physical meaning of toughness and of how toughness depends on microstructure, strain rate, temperature, and so forth, is still insufficient. This understanding can best be improved by developing computational models capable of describing the fracture process realistically and in detail.

To derive theoretical expressions that would accurately describe microfracture activity at the tip of a propagating crack is a major task. A number of models postulated for microfracture nucleation at inclusions or on cleavage planes, for plastic void growth, and the like, are in principle capable of describing the fracture process for a given material under given load conditions (usually in the necking region of a tensile bar). Also, it might be possible to combine certain nucleation and growth models to yield predictions of void size distributions for arbitrary load histories. However, many of the parameters used in the current models may not have a physically realistic basis. For example, it is unclear whether inclusion/matrix decohesion is controlled by shear stress, shear strain, normal stress, or some combination. Furthermore, no satisfactory model for microfracture coalescence appears to exist. Thus a successful theoretical model of microfracture nucleation, growth, and coalescence remains to be developed.

An approach that may have higher chances of early success is the observational approach used to develop a predictive capability for fracture under short impulse loads.[7] The fracture damage produced by a tensile pulse is quantitatively assessed by counting and measuring the size of individual microfractures visible on polished cross sections of impacted specimens. Figure 2 shows microcracks produced in Armco iron by planar impact (note their similarity to the microfractures shown in Figure 1.) The large number of microfractures makes a statistical approach possible,

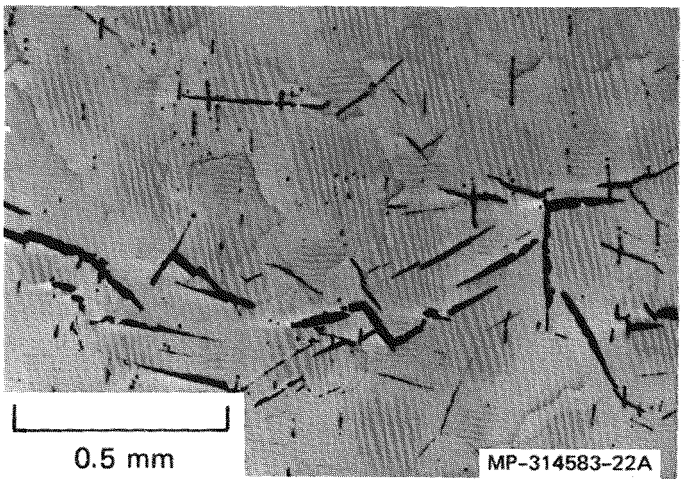

FIGURE 2 MICROCRACKS IN ARMCO IRON INDUCED BY IMPACT

and damage distribution functions can be constructed. By correlating these data with the loading history, we obtain empirical expressions describing nucleation and growth rates. Thus the approach is not to consider mechanistic details of nucleation and growth, such as the size distribution or spacing of nucleation heterogeneities, or the dislocation models describing how voids grow, but rather to deduce the microfracture nucleation and growth laws directly from the measured microfracture data. This approach is known as the SRI NAG approach.

Applications of the SRI NAG approach to a variety of ductile and brittle metals and alloys [7-10] showed that microfractures nucleate and grow (NAG) according to the expressions

$$\dot{N} = \dot{N}_o \exp \frac{\sigma - \sigma_{no}}{\sigma_1} \tag{1}$$

$$\dot{R} = \frac{\sigma - \sigma_{go}}{4\eta} R \tag{2}$$

where the nucleation rate $\dot{N}$ is an exponential function of the tensile stress σ, and the growth rate $\dot{R}$ depends linearly on the stress and the size of the microfracture R. The remaining parameters act as material properties describing various aspects of micromechanical behavior. Their values are fixed by the fit to the data.

III COMPUTATIONAL APPROACH

The purpose of this program was to determine whether the microfracture nucleation and growth functions extracted from plate impact experiments could be used to describe microfracture activity ahead of a propagating crack, and thereby allow a direct determination of the absorbed energy, i.e., the fracture toughness. We, therefore, performed a computational simulation of an actual DCB crack arrest experiment by using the SRI NAG model and dynamic fracture data from plate impact experiments. A two-dimensional wave propagation code was used to compute the stress histories experienced by the material at the moving crack tip.

As a test case, we selected the DCB crack arrest experiment 3V-31 performed by Battelle Memorial Institute.[11] The specimen was a rectangular, notched plate of 4340 quenched and tempered steel with no side grooves. Specimen geometry and wedge loading arrangement are shown in Figure 3. Loading pins were inserted in the holes at the notched end of the specimen, and a wedge attached to the crosshead of a tensile machine was forced downward between the pins. At constant crosshead speed, the load on the specimen increased monotonically until a sharp crack advanced from the blunted notch and propagated into the specimen. The crack ran about 75 mm at an average constant velocity of 435 m/s, then abruptly stopped. Wedge opening load and displacement at the onset of crack propagation were measured; crack velocities were measured by monitoring the breakage of a grid of conducting strips cemented across the expected crack path. Since the crack speed was orders of magnitude greater than the wedge opening rate, essentially fixed grip conditions prevailed. Reference 11 gives additional details.

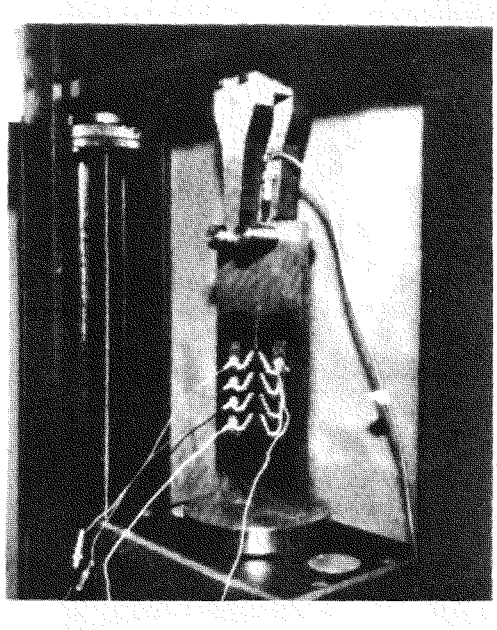

(a) WEDGE LOADING ARRANGEMENT FOR DCB SPECIMEN SHOWING THE VELOCITY MEASURING CONDUCTING STRIPS

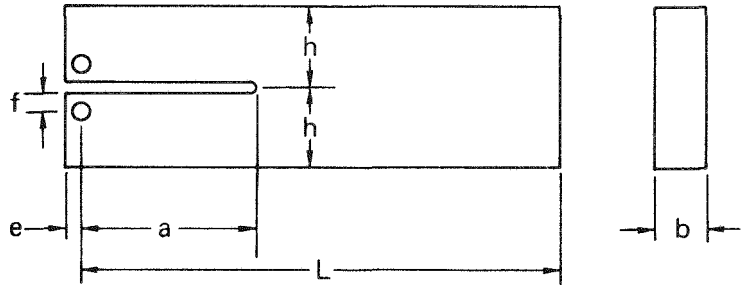

a_o = 2.670 in. (67.8 mm) f = 0.80 in. (20.3 mm)
b = 0.500 in. (12.7 mm) h = 2.500 in. (63.5 mm)
e = 0.63 in. (16.0 mm) L = 11.36 in. (305.0 mm)
Pin Diameter 1.00 in (25.4 mm)

(b) DIMENSIONS OF TEST PIECES

MP-314583-23A

FIGURE 3 WEDGE LOADING ARRANGEMENT AND SPECIMEN DIMENSIONS FOR THE DOUBLE CANTILEVER BEAM CRACK ARREST EXPERIMENT

The dimples on the fracture surfaces, Figure 4(a), were approximately equiaxed and their diameters varied by up to several micrometers. The absence of isolated voids beneath the fracture surfaces, Figure 4(b), and in front of the main crack tip indicates that voids form only in a very small zone ahead of the advancing crack tip and that all voids that nucleate become part of the main fracture. Further results of metallographic and fractographic examination of this specimen are reported in Appendix A.

Fast crack propagation through a material is clearly a dynamic process. Since the load is applied at some distance from the crack tip, stress information must be continually transmitted through the specimen as the crack runs. This is accomplished by stress waves. Consider the loaded DCB specimen at the point of instability. As the crack starts to run, the stresses at the crack tip relax somewhat and the crack tends to slow or stop. This unloading information is communicated to the load point by way of a stress wave, and new load information runs back to the crack tip and builds up the stress concentration. The crack may respond by accelerating again, thereby relaxing the stresses. This cycle may repeat itself many times. Arrest occurs when stress relaxation resulting from crack extension is such that the applied load can no longer maintain fracture. Such stop-and-go crack propagation and corresponding stress wave activity have been observed by Van Elst,[12,13] who used ultrahigh-speed photographic and electronic methods to demonstrate the intermittent nature of crack propagation. He found that fracture proceeded in a series of discrete steps and that sizeable stress waves emanated from the crack tip at each advance.

Thus, the stresses at a propagating crack tip vary with time in an oscillatory manner and require a wave propagation code for an accurate accounting. Kanninen,[14] Schmuely and Peretz,[15] and Wilkins (private communication) have applied one-, two-, and three-dimensional wave propagation codes, respectively, to the DCB geometry. In the work reported

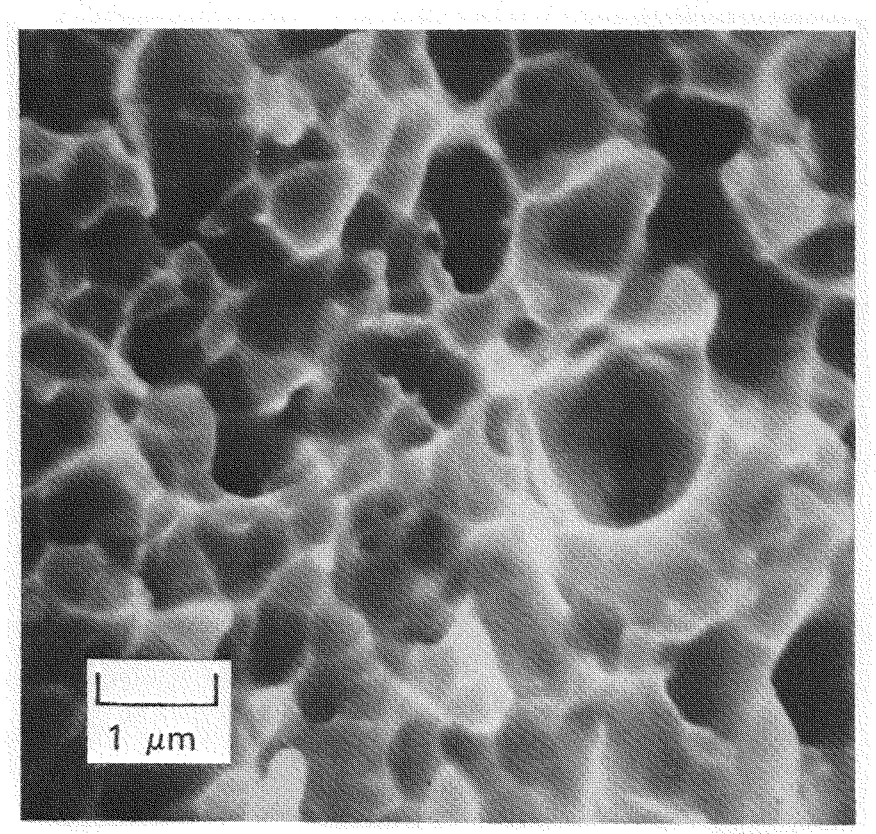

(a) DIMPLED FRACTURE SURFACE

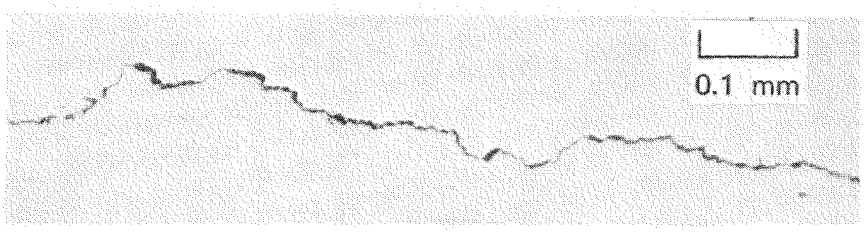

(b) SCALLOPED SIDE PROFILE

MP-4405-10

FIGURE 4 FRACTURE TOPOLOGY OF CRACK ARREST SPECIMEN

here, the stress distribution in the specimen at all points in time was calculated by use of TOODY3,[16] a two-dimensional, Lagrangian, finite difference wave propagation code. Plane strain conditions were assumed. This code solves equations for conservation of mass, momentum, and energy in two space dimensions at successive, small (0.5 μs) time steps and computes thereby the two-dimensional strain and stress states. A simple constitutive equation for the material was constructed using nonstandard round bar tensile data from specimens machined from the broken halves of the DCB specimen.

The computational grid consisted of a 16 x 50 array of 4.0 x 6.4 mm cells, as indicated in Figure 5. Because of symmetry, only half of the specimen had to be considered. Although a much finer grid with cell sizes of the order of the dimple size would be required for accurate results, we chose the coarse grid of Figure 5 to provide a less expensive feasibility demonstration.

The computation was accomplished in two stages. First, the measured wedge opening displacements and forces were applied to the computational grid to obtain the elastic stress distribution in the specimen at the point of instability by use of the method of dynamic relaxation, described in Appendix B. When the static elastic solution was obtained to within one percent, yielding was allowed to occur.

The second calculational stage began with instability of the blunted notch and continued until many microseconds after arrest. In this stage, stress wave activity was computed and allowed to dictate the stress state and fracture activity at the propagating crack tip. Nucleation and growth of voids was treated as occurring according to Equations (1) and (2) (page 9). Nucleation and growth rate parameters for cracks in a similar steel under plate impact loading conditions were assumed applicable.[10] As microfractures nucleate and grow in a cell, the cell gradually weakens. Coalescence of microfractures was

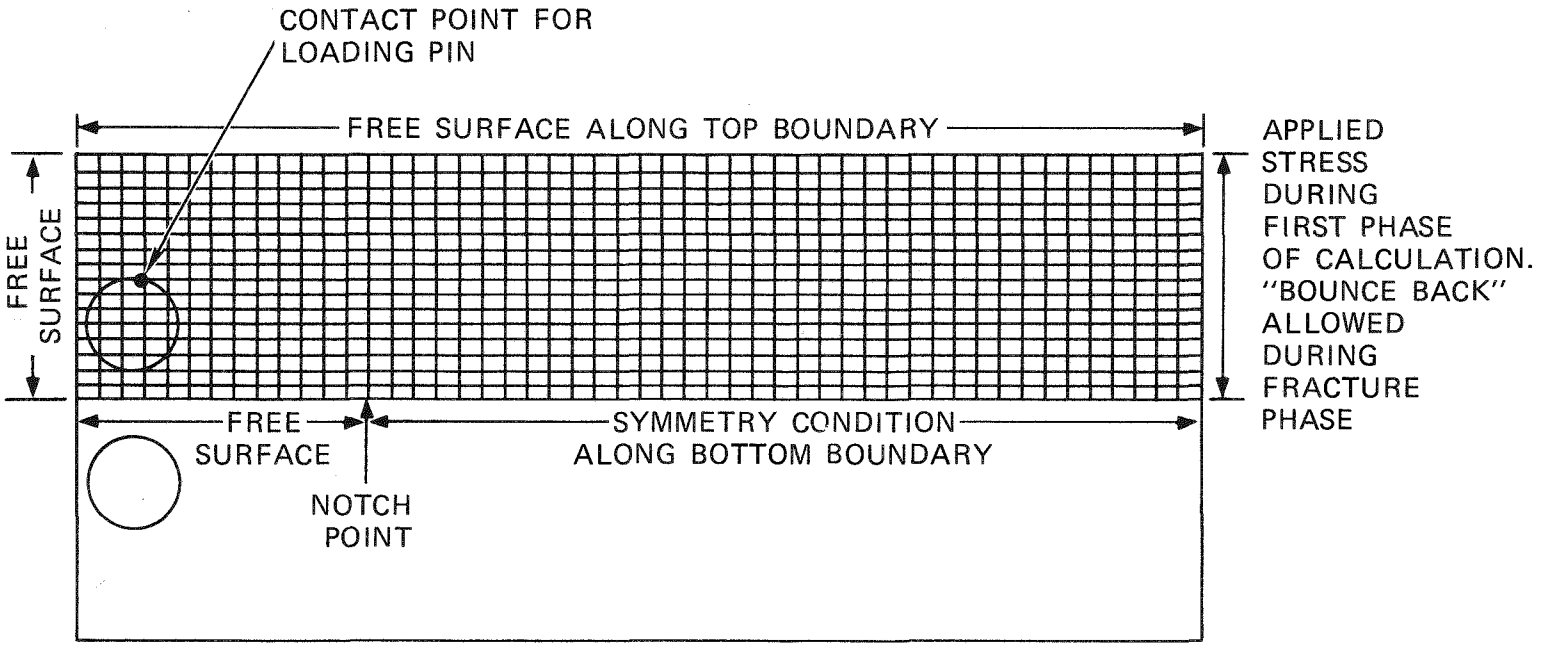

FIGURE 5 GRID SCHEME AND BOUNDARY CONDITIONS USED IN COMPUTATION

computed when their number and sizes reached a specified critical level. Cell rupture was assumed to occur and the crack to advance one cell length when the volume of all fragments generated by the coalescing microfractures equaled the volume of the computational cell. Thus, the crack velocity is defined by the rate at which successive cells rupture. Appendix C describes how the fracture subroutine BFRACT is inserted into the wave propagation code.

Crack branching was calculated as soon as instability occurred. A propagating fracture occurred along the specimen midplane, and a crack began to propagate at right angles to it. Although bifurcation and trifurcation of fracture in similar specimens are frequently observed,[17] the crack in the particular Experiment 3V-31 simulated here propagated nominally on the specimen midplane. A second calculation was then performed for which off-axis cells were not permitted to fracture. The calculated crack ran 51.4 mm, about one-third of the experimentally observed arrest length, in about 65 μs before stopping. The calculation was continued for an additional 100 μs after arrest to test whether reinitiation would occur. The propagation velocity was rather constant at 790 m/s, about 80 percent higher than measured. There were no significant periodic oscillations in macrocrack velocity from the periodic stress wave loading.

The energies absorbed in microfracturing and by plastic flow at the crack tip were calculated and printed out. The microfracturing energy was computed at each time step as the product of the average stress in the cell and the change in cell volume resulting from the nucleation and growth of microfractures during that time step. Similarly, the plastic energy was computed as the stress times the plastic strain.

The variation with time of the elastic strain energy and the energies absorbed by plastic flow and microcracking are shown in Figure 6 for the material in the seventh computational cell from the notch point. As the crack tip approached and loaded this cell, the elastic strain energy rose sharply. Plastic flow soon occurred, and the crack tip material began to absorb the elastic energy. Microfracturing, begun somewhat later, ruptured the cell after about 25 μs.

The results show that relatively little energy is absorbed in the microfracturing process; about 20 times as much is absorbed in plastic flow. However, the microfracturing activity ruptures the cell and thus controls the amount of plastic energy absorbed. Figure 6 shows the crescendo of microfracturing activity shortly before it ruptures the cell.

The rupture of this particular crack tip cell required 86 MN/m^2 of plastic work and only 3.3 MN/m^2 of microfracturing work. Thus, the fracture toughness derives largely from plastic flow at the crack tip. If we assume that the radius of the plastic zone at the midplane of the specimen is 10^{-4} m, we can compute and convert the energy absorbed per unit crack extension to obtain the fracture toughness for a propagating crack K_{ID}. The resulting value $K_{ID} = 61\ MNm^{-3/2}$ for a velocity of 790 m/s compares favorably with reported values[11] for static initiation toughness and arrest toughness of 54 $MNm^{-3/2}$ and 68 $MNm^{-3/2}$, respectively. In view of the coarseness of the computational grid and the approximate nature of the microfracture properties and constitutive relations, however, this result should be considered preliminary.

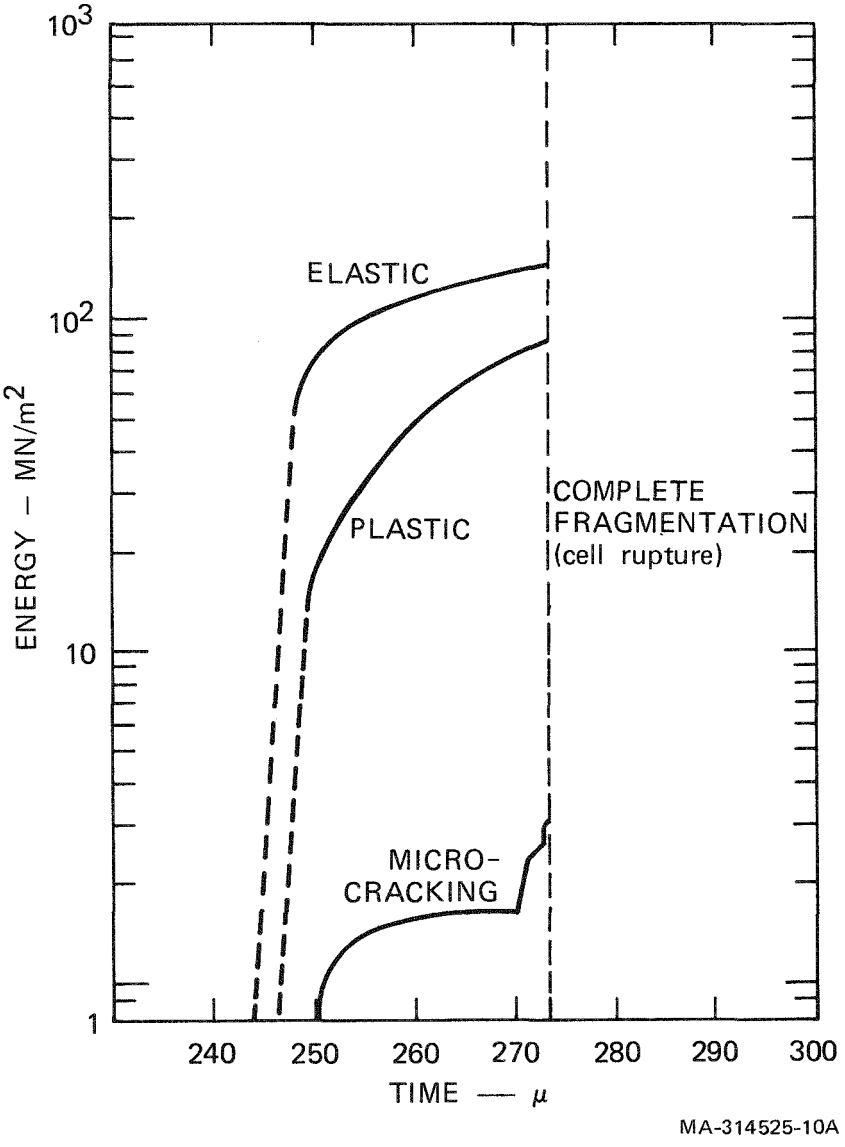

FIGURE 6 ENERGY PARTITIONING IN A COMPUTATIONAL CELL IN A DCB SPECIMEN AS THE CELL IS TRAVERSED BY THE CRACK

IV DISCUSSION OF RESULTS

We have demonstrated the feasibility of computing the energies absorbed at the tip of a propagating and arresting crack by treating the microevents that occur in the process zone. Agreement with experimental measurements of crack velocity and arrest length would be improved by using a finer computational grid to more accurately resolve the crack tip stress concentration and to concentrate the fracture damage in a zone comparable in size to the process zone. This should decrease the macrocrack velocity and reduce the tendency for branching. The use of more accurate nucleation and growth properties and constitutive equations would further improve agreement with experimental measurements.

The use of more detailed and physically realistic models to compute crack propagation and arrest would provide a link between continuum mechanics parameters and microscopic material behavior. For example, being able to derive the fracture toughness from known individual contributing factors on the microstructure level, such as plastic energy and microfracture energy, would be a great advance. Also, the more detailed approach used here is not restricted by geometry, strain rate,* or even stress state. Therefore, the results of detailed calculations may be helpful in extending the use of simple continuum approaches to more ductile materials and to smaller specimens. Finally, this approach would permit the role of microstructure in controlling toughness to be studied and perhaps understood in a more quantitative way.

---

*Simple trial calculations on a one-dimensional array of cells in triaxial tension indicate that the microfracture energy depends strongly on strain rate, Appendix D.

Of immediate interest is whether the toughness exhibited by a material in arresting a running crack can be considered a material property, as suggested by Crosley and Ripling,[1] or if the arrest toughness is significantly influenced by stored kinetic energy and thus has little meaning as a material property, as suggested by Hahn et al.[2] An understanding of the energy partitioning among the various microprocesses occurring at crack arrest would be helpful in resolving this question. The detailed physically realistic calculations described here can provide such energy partitioning information.

V REFERENCES

1. P. B. Crosley and E. J. Ripling, Nuclear Engineering and Design, Vol. 17, 1971, p. 32.

2. G. T. Hahn, R. G. Hoagland, M. F. Kanninen, and A. R. Rosenfield, Proceedings of Second International Conference on Pressure Vessel Technology, San Antonio, Texas 1973, p. 995.

3. C. Crussard, J. Plateau, et al. in Fracture, B. L. Averbach et al., eds. (Wiley, New York, 1959), p. 524.

4. R. G. Hoagland, A. R. Rosenfield, and G. T. Hahn, Metallurgical Transactions, Vol. 3, 1972, p. 123.

5. T. B. Cox and J. R. Low, Jr., Metallurgical Transactions, Vol. 5 1974, p. 1457.

6. I. G. Palmer and G. C. Smith, Proceedings AIME Conference on Oxide Dispersion Strengthening, Bottom Landing, New York, June 1966, (Gordon and Breach, New York, 1967).

7. T. W. Barbee, Jr., L. Seaman, R. Crewdson, and D. Curran, Journal of Materials, Vol. 7, 1972, p. 393.

8. D. A. Shockey, L. Seaman, and D. R. Curran, Final Technical Report AFWL-TR-73-12, Kirtland Air Force Base, New Mexico, 1973.

9. D. A. Shockey, L. Seaman, and D. R. Curran et al., Final Technical Report on Contract DAAD05-73-C-0025, U.S. Army Ballistic Research Laboratories, Aberdeen, Maryland, 1973.

10. L. Seaman and D. A. Shockey, Final Technical Report AMMRC CTR 75-2, Army Materials and Mechanics Research Center, Watertown, Massachusetts, 1975.

11. G. T. Hahn, R. G. Hoagland, M. F. Kanninen, and A. R. Rosenfield, Dynamic Crack Propagation, G. C. Sih, ed., (Noordhoff International Publishing, Leyden, 1972), p. 649.

12. H. C. Van Elst, Transactions American Institute Metallurgical Engineers, Vol. 230, 1964, p. 460.

13. H. C. Van Elst, Dynamic Crack Propagation, G. C. Sih, ed., (Noordhoff International Publishing, Leyden, 1972), p. 283.

14. M. F. Kanninen, International Journal of Fracture, Vol. 10, 1974, p. 415.

15. M. Schmuely and D. Peretz, International Journal of Solids and Structures, Vol. 12, 1976, p. 67.

16. L. D. Bertholf and S. E. Benzley, Sandia Laboratory Research Report SC-RR-68-41, 1968.

17. G. T. Hahn et al., First Annual Progress Report on Task Agreement No. 62, Battelle Columbus Laboratories, Ohio, BMI-1937 NRC-5, 1975.

18. J.R.H. Otter, A. C. Cassell, and R. E. Hobbs, Dynamic Relaxation, Proceedings of the Institute of Civil Engineering, Paper No. 6986, 1967.

Appendix A

METALLOGRAPHIC AND FRACTOGRAPHIC EXAMINATION OF SPECIMEN 3V-31

Fracture Surface Examination

Fracture surfaces and various polished cross sections from Battelle DCB Specimen 3V-31 were examined by optical and scanning electron microscopy. The objective was to obtain information on the micromechanism of fracture and to determine the role of microstructural features such as inclusions and grain boundaries.

Figure A-1 shows the adjacent fracture surfaces from the starting hole to a point approximately 2 cm from the arrest site. Initiation occurred at a point along the starter hole about 20% in from one side. Evidence of jerky crack motion is not obvious, although the regularly spaced deep gouges near the specimen sides have not yet been interpreted. Shear lip depth seems to be constant.

At slightly higher magnification, less visible features of the fracture surface become discernible. Figure A-2 shows the existence of cracks and grooves oriented parallel to the propagation direction. These features are probably manifestations of material weak spots induced by the rolling operation. The cracks indicate that the stresses through the thickness are significant.

The main crack clearly propagates by a ductile hole growth mechanism, at least until near the arrest site. Figure A-3 shows higher magnification views of the fracture surface. The dimpled texture indicative of coalesced voids is obvious.

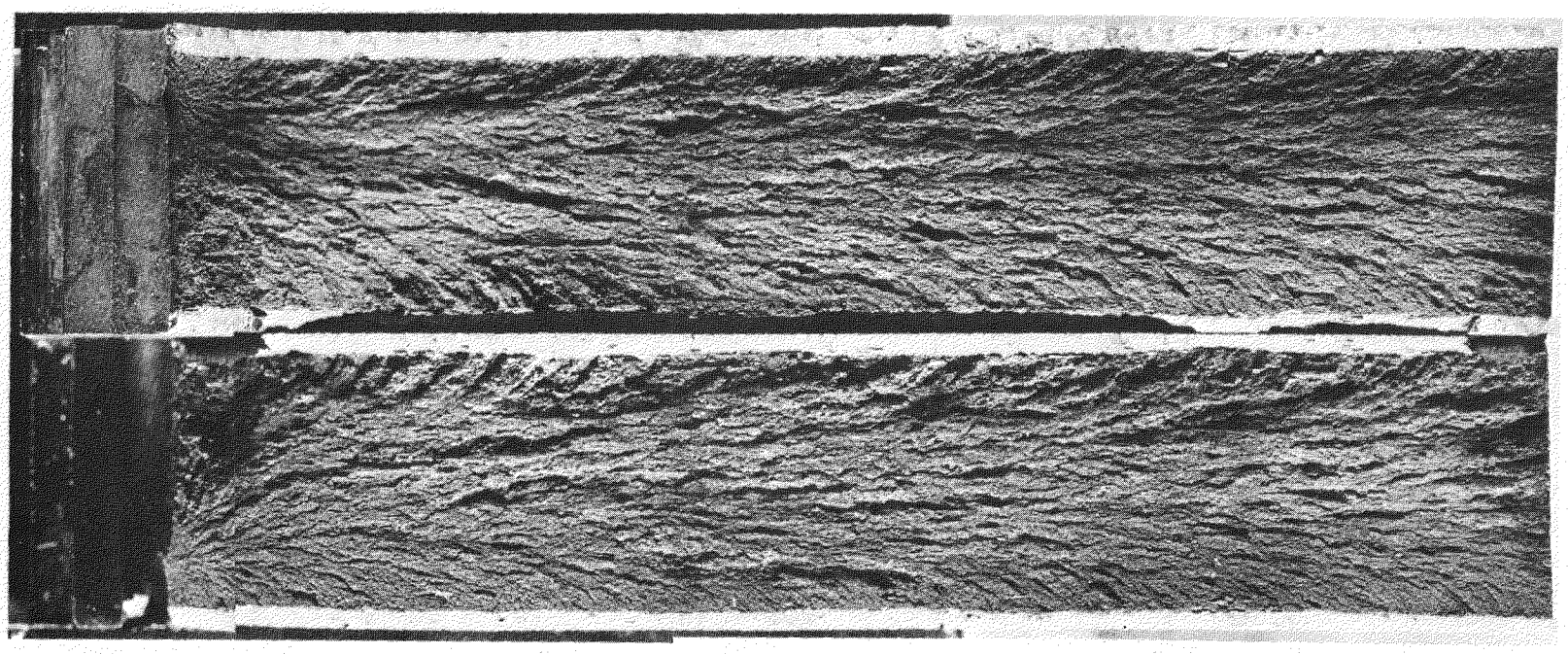

FIGURE A-1 FRACTURE SURFACES OF BATTELLE DCB SPECIMEN 3V-31 FROM STARTER HOLE TO ABOUT 2 cm FROM ARREST SITE

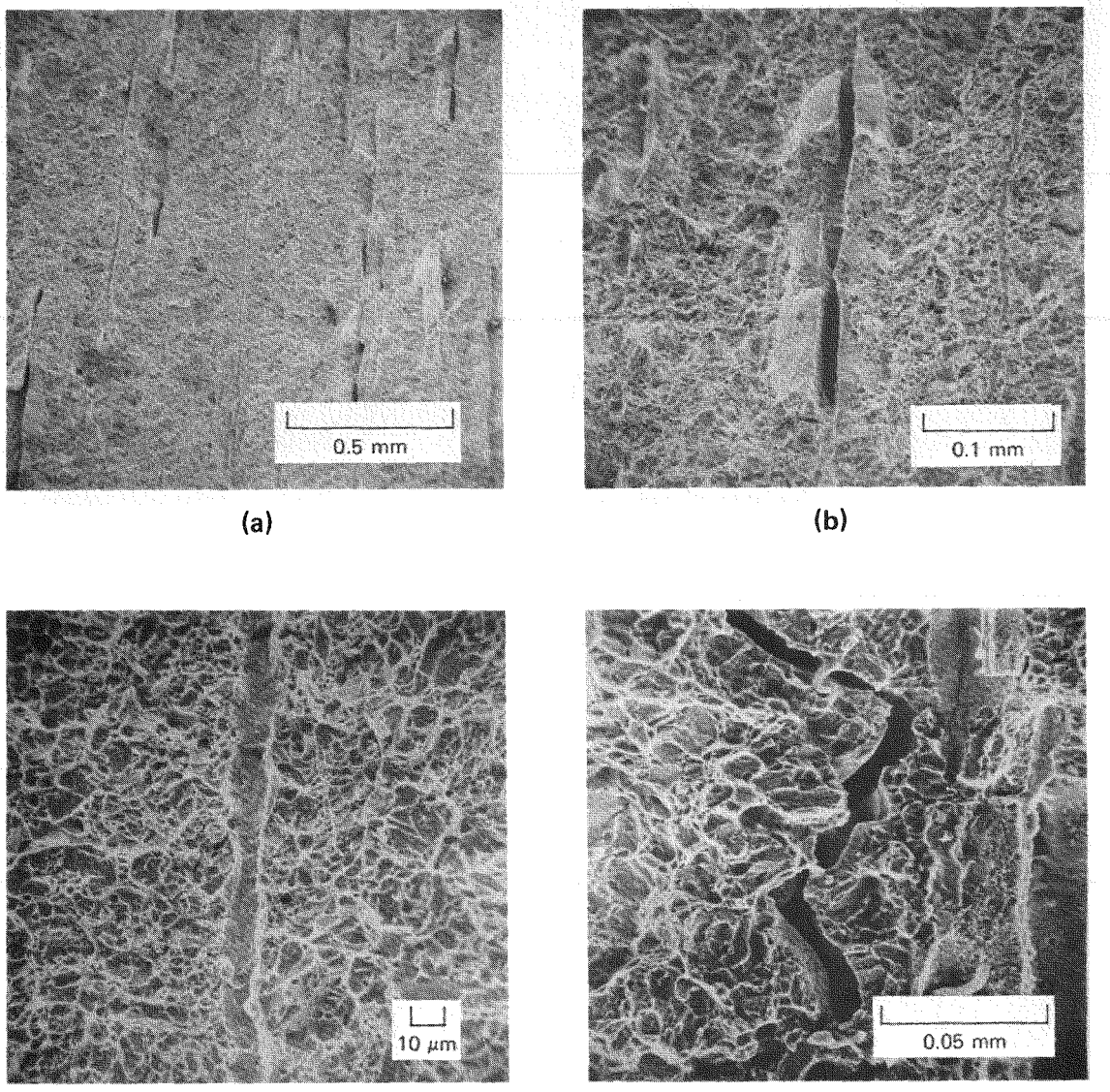

FIGURE A-2 CRACKS AND GROOVES ON FRACTURE SURFACE

Propagation direction of main crack was from top to bottom.

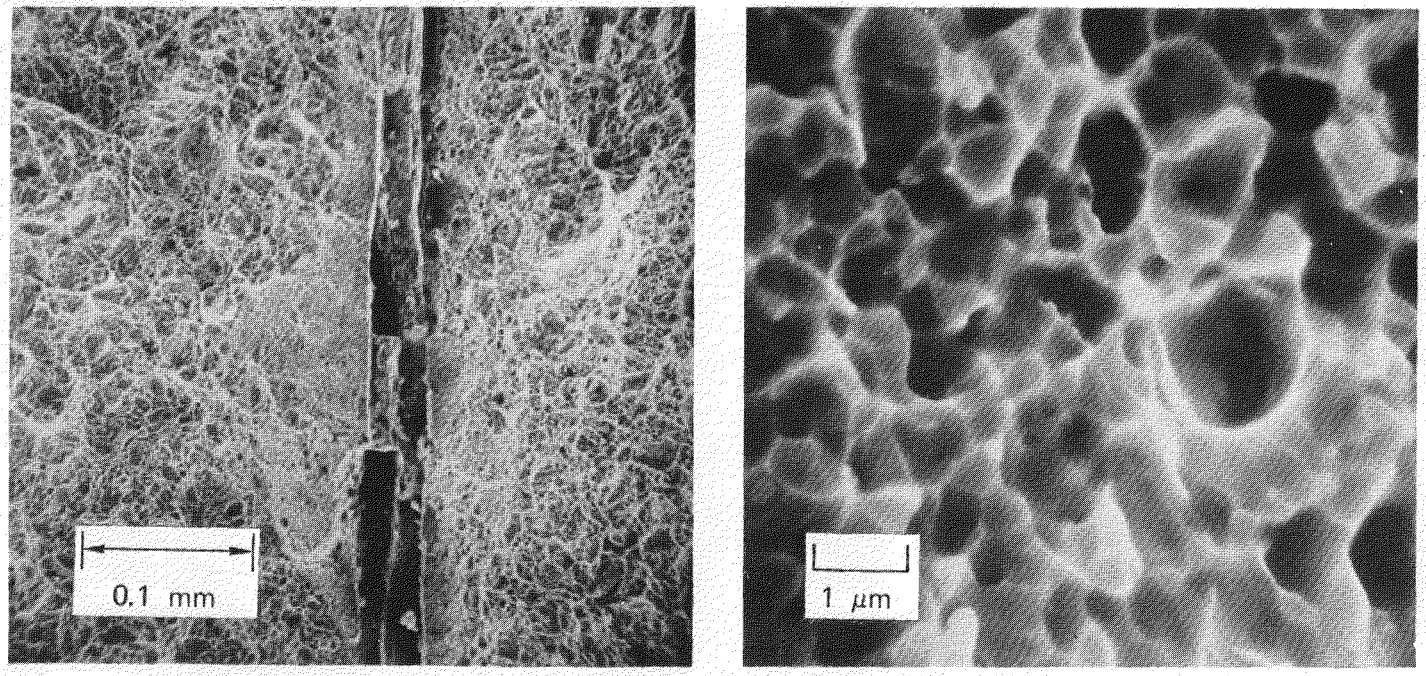

MP-4405-3

FIGURE A-3 SCANNING ELECTRON MICROGRAPHS SHOWING DUCTILE DIMPLED NATURE OF FRACTURE SURFACE

Examination of Polished Sections

The dimpled fracture surface texture is also evident in profiles of the fracture surface on polished sections perpendicular to the crack plane. The specimen was sectioned with a glasscutter's saw (Figure A-4). These surfaces were then polished and sometimes etched in preparation for microscopic examination. Figure A-5 shows the scalloped profile of the fracture surface from a side-on and an end-on view. We conclude that the main crack propagated by the nucleation, growth, and coalescence of ductile spherical microvoids, which appears to be the only way such a surface morphology could be produced.

Near the crack arrest site, however, the main crack profile has a different appearance, as shown in Figure A-6. Instead of the rounded scalloped profile shown in Figure A-5, we observe a straight-edged, angular, zigzag profile. Closer examination of the etched surface indicates that the crack path follows boundaries of prior austenite grains, and further, that the crack exhibits a tendency to branch and wander from the nominal path, Figure A-6. Thus, either the fracture mode changes from a ductile microvoid mode to planar grain boundary failure as the crack slows to arrest, or grain boundary rupture is always the initial failure mode, but the grain boundary cracks become void-shaped due to stretching at their tips as the DCB arms move apart.

Little evidence was found of unconnected microfractures ahead of

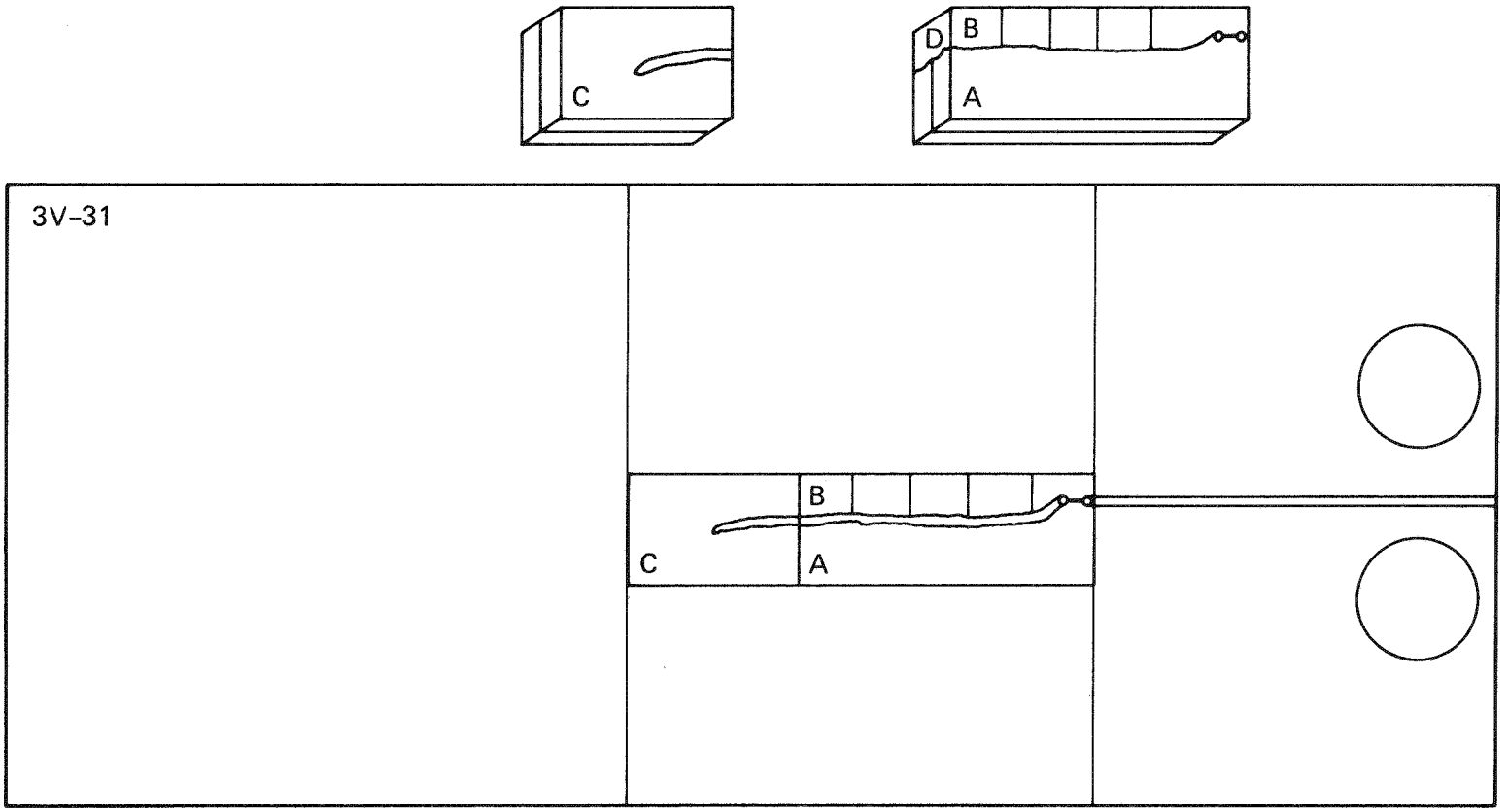

FIGURE A-4 SKETCH OF SECTIONS CUT FOR METALLOGRAPHIC EXAMINATION FROM BATTELLE DCB CRACK ARREST SPECIMEN 3V-31

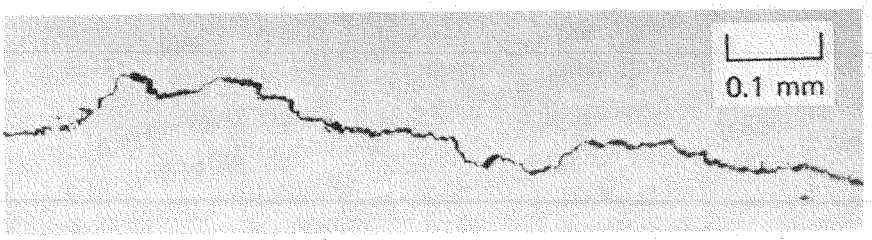

(a) SIDE-ON

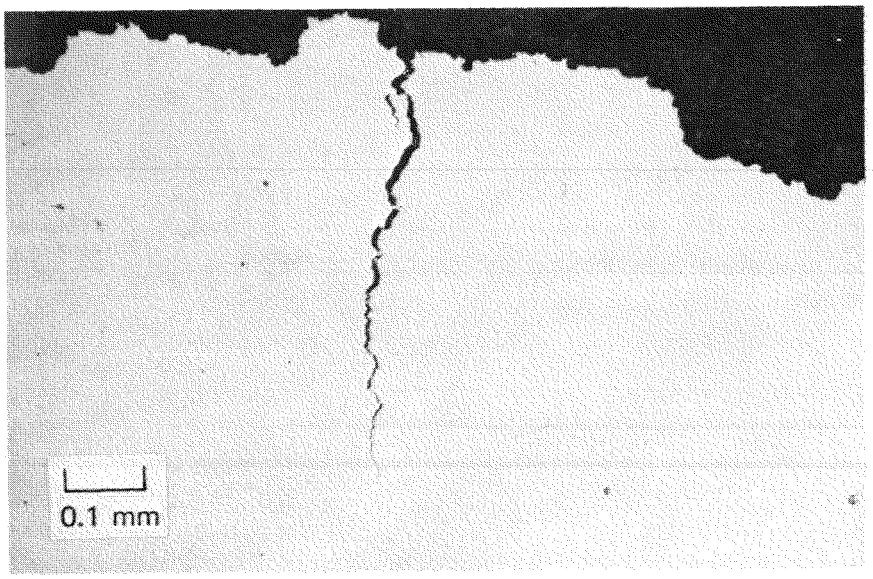

(b) END-ON

MP-4405-5

FIGURE A-5 VIEWS SHOWING SCALLOPED PROFILE OF CRACK

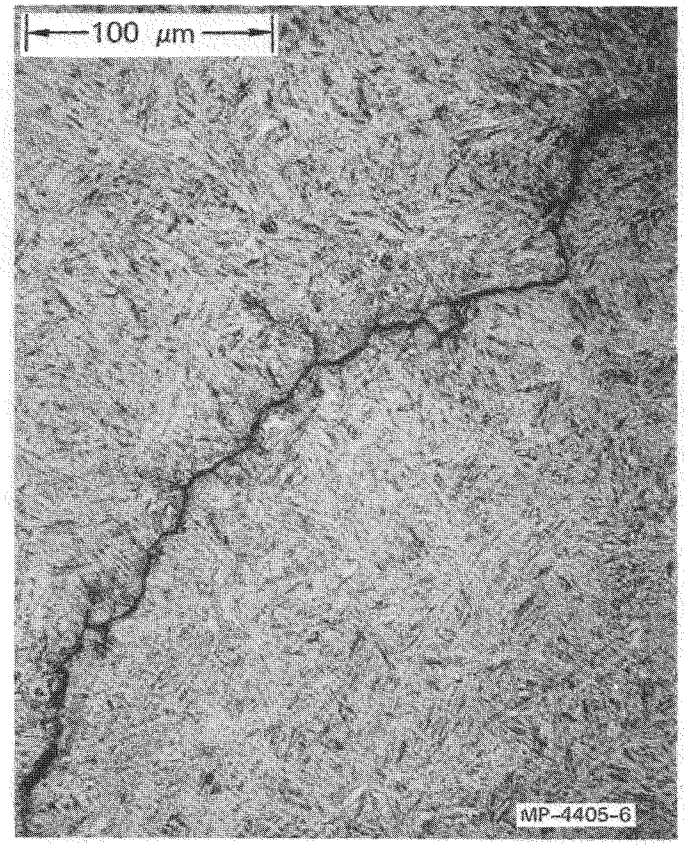

NOTE: Planar appearance of crack segments, preference of crack to follow prior austenite grain boundaries, and tendency of crack to bifurcate.

FIGURE A-6 POLISHED AND ETCHED CROSS SECTION SHOWING CRACK NEAR THE ARREST SITE

or adjacent to the main crack. Even inclusions near the path of the main crack appeared generally undamaged, although inclusions are known to be microcrack initiation sites.

Perhaps the most unexpected result was the appearance of cracks on either side and in advance of the main crack on planes normal to the main crack propagation direction. Figure A-7 represents a polished mid-specimen section showing the distribution of these cracks along the main crack path. These cracks occur in greater number near the initiation and arrest sites, are typically 1 to 5 mm long, and are intergranular. Only those cracks near the arrest site intersect the main crack; those elsewhere appear to lie 2 mm or more away. One large crack is observed in advance of the main crack tip. Such cracks represent a mechanism for branching and for the arm-break-off phenomenon reported under certain conditions of DCB testing.

Summary of Findings from Metallographic Examination

The results of our metallographic examination can be summarized as follows:

- Macrocrack advancement in the DCB specimen examined apparently occurred by nucleation, growth, and coalescence of ductile spherical microvoids.

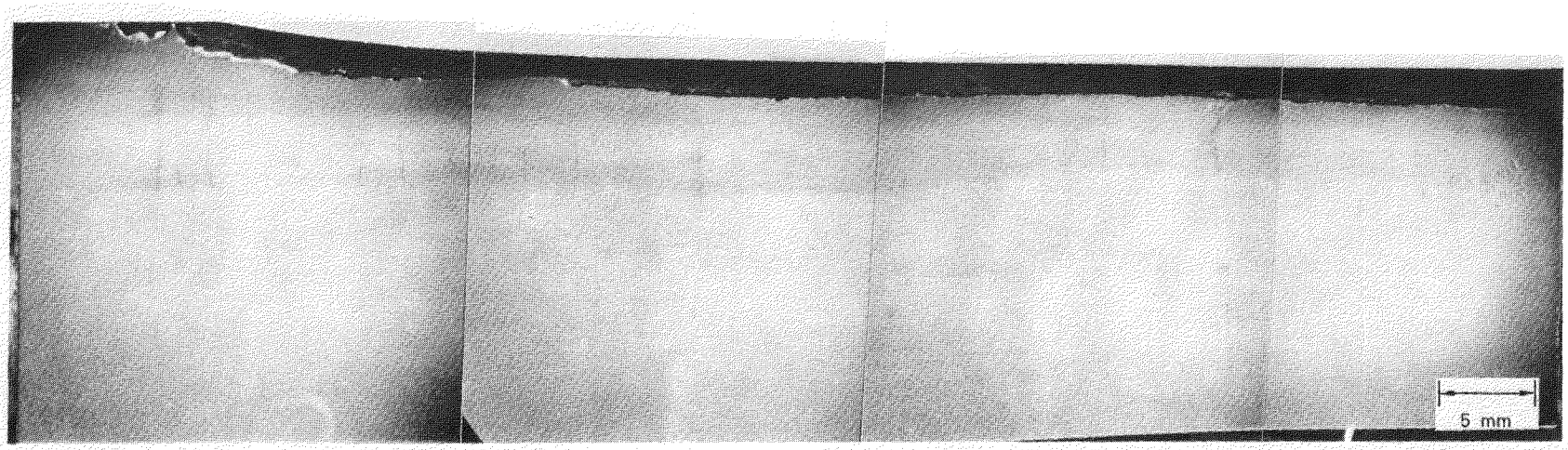

(a) REGION CONTAINING STARTER HOLE (ETCHED)

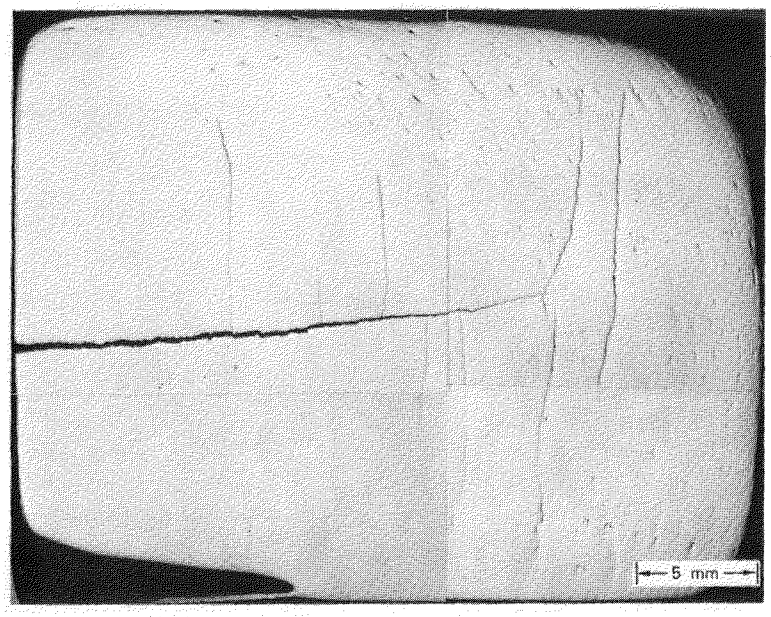

(b) REGION CONTAINING CRACK ARREST SITE (UNETCHED)

MP-4405-7

FIGURE A-7 MID SPECIMEN CROSS SECTIONS NORMAL TO PIN AXIS SHOWING CRACKS ADJACENT TO MAIN CRACK

- The fracture mode appeared to change to intergranular failure near the arrest site, although grain boundary cracks may be a precursor to ductile voids.
- Intergranular cracks several millimeters long were observed on either side of and in advance of the main crack normal to the main crack plane.

Appendix B

DYNAMIC RELAXATION

Dynamic relaxation is a method for using wave propagation computer programs to obtain solutions to static problems. This appendix describes the method and reports on preliminary results of its application.

Static problems of structures are usually solved by the simultaneous solution of a series of equilibrium equations. In recent years, large computer programs called finite element codes have been built to solve such static problems. Such calculations become very expensive when

- The material behavior is so nonlinear that the program must proceed by a series of steps to the final solution.
- The matrix of coefficients in the simultaneous equations must be reevaluated at each step.
- The number of elements is large.

Under such conditions a wave propagation code may provide a faster solution. The wave propagation codes operate by explicit, finite-difference methods not requiring large matrix inversion. With explicit methods, extremely general material behavior can be readily accommodated.

Background

Dynamic relaxation was developed several years ago for solving static problems with large scale structures. In its early development,

Otter[1,2]* envisioned the method as a means of speeding up finite element calculations by introducing an iteration procedure. Several related methods have been used to modify wave propagation codes to use the dynamic relaxation technique. Andrews and Hancock[3] presented such a method in 1972 and Hancock[4] described a simpler approach in 1973. The Hancock method, which appears to be identical to that of Otter, is used here.

Derivation of Equations

The dynamic relaxation method requires adding a velocity term to the momentum equation. Conservation of momentum normally leads to an equation of the form

$$\frac{\partial^2 U_i}{\partial t^2} = \frac{\Sigma F_i}{M} \tag{B-1}$$

where U_i is displacement in the i direction, ΣF_i is the summation of forces in the i direction, and M is the mass. Equation (B-1) is normally integrated in time to determine the velocity

$$\dot{U}_i^{n+\frac{1}{2}} = \dot{U}_i^{n-\frac{1}{2}} + \frac{\Sigma F_i^n \Delta t}{M} \tag{B-2}$$

*References are listed at end of Appendix B.

where $\underline{\dot{U}}^{n+\frac{1}{2}}$ is the normally computed velocity at time $n + \frac{1}{2}$

$\dot{U}^{n-\frac{1}{2}}$ is the velocity at the time $n - \frac{1}{2}$

F_i^n is the force at time n

Δt is the time step.

For dynamic relaxation, the momentum equation is augmented by a velocity term

$$\frac{\partial^2 U_i}{\partial t^2} + \frac{2}{\tau}\frac{\partial U}{\partial t} = \frac{\Sigma F_i}{M} \tag{B-3}$$

where τ is a time constant for the relaxation process. Equation (B-3) is discretized to obtain velocity

$$\dot{U}_i^{n+\frac{1}{2}} = \dot{U}_i^{n-\frac{1}{2}} + \left(\frac{\Sigma F_i^n}{M} - \frac{2\dot{U}_i^n}{\tau}\right)\Delta t \tag{B-4}$$

Now, let $\dot{U}_i^n = \frac{1}{2}\left(\dot{U}_i^{n-\frac{1}{2}} + \dot{U}_i^{n+\frac{1}{2}}\right)$ (B-5)

and solve Equation (B-4) for $\dot{U}_i^{n+\frac{1}{2}}$

$$\dot{U}_i^{n+\frac{1}{2}} = \left(\frac{2}{1 + \frac{\Delta t}{\tau}} - 1\right)\dot{U}_i^{n-\frac{1}{2}} + \frac{1}{1 + \frac{\Delta t}{\tau}} \cdot \frac{\Sigma F_i^n \Delta t}{M} \tag{B-6}$$

Then, replace F_i^n by its value from Equation (B-2).

$$\dot{U}^{n+\frac{1}{2}} = \frac{1}{1 + \frac{\Delta t}{\tau}}\underline{\dot{U}}^{n+\frac{1}{2}} + \left(\frac{1}{1 + \frac{\Delta t}{\tau}} - 1\right)\dot{U}^{n-\frac{1}{2}} \tag{B-7}$$

Equation (B-7) is particularly convenient, because it contains only the normally computed velocity, the velocity at the previous step, and the adjusted velocity. Thus, to use dynamic relaxation, one obtains $\underline{\dot{U}}$ with the usual computational scheme and then computes $\dot{U}$ from Equation (B-7). Hence, Equation (B-7) is simply added to existing wave propagation codes to permit dynamic relaxation calculations. For obtaining critical damping, τ should correspond to the lowest mode of oscillation. For a wave propagation problem, τ should be proportional to L/C, where L is the greatest length in the problem and C is the sound speed.

The next step is to determine appropriate values of τ to induce critical damping. For this purpose, rewrite Equation (B-7) as follows:

$$\dot{U}_i^{n+\frac{1}{2}} = \left(1 - \frac{\frac{\Delta t}{\tau}}{1 + \frac{\Delta t}{\tau}}\right) \underline{\dot{U}}_i^{n+\frac{1}{2}} - \frac{\frac{\Delta t}{\tau}}{1 + \frac{\Delta t}{\tau}} \dot{U}_i^{n-\frac{1}{2}} \qquad \text{(B-8)}$$

Let the common coefficient be

$$\frac{\frac{\Delta t}{\tau}}{1 + \frac{\Delta t}{\tau}} \doteq \frac{\beta \Delta t}{T} \qquad \text{(B-9)}$$

where β is a constant and T is the propagation time, L/C.

Now Equation (B-8) takes the form

$$\dot{U}_i^{n+\frac{1}{2}} = (1 - \frac{\beta \Delta t}{T}) \underline{\dot{U}}_i^{n+\frac{1}{2}} - \frac{\beta \Delta t}{T} \dot{U}_i^{n-\frac{1}{2}} \qquad \text{(B-10)}$$

The problem now reduces to obtaining appropriate values of β. Tests to find the best value are now described.

Sample Relaxation Calculations

Dynamic relaxation calculations were performed with the one-dimensional code SRI PUFF to examine convergence of the method and to optimize the relaxation constant. The problem chosen is simply compression of a sample confined to a planar, one-dimensional strain geometry. The material was treated as a column of 20 cells, pressure was applied at one end, and the other end was fixed. Three computational conditions were considered:

- All cells of equal size to examine the usual case with several values of β.
- All cells of equal size, but of a linearly varying velocity initialized throughout.
- The two bottom cells divided in thirds to provide six small cells in addition to eighteen regular sized cells to examine the effect of a reduced time step on the rate of convergence.

The computations were performed with several values of β to find the optimum value. The results of several of the computations are shown in Figure B-1. In each case, the stress near the top of the column approaches the applied stress (1.0) very rapidly, levels off, and then more gradually approaches 1.0. For a low value of β, the stress oscillates about 1.0.

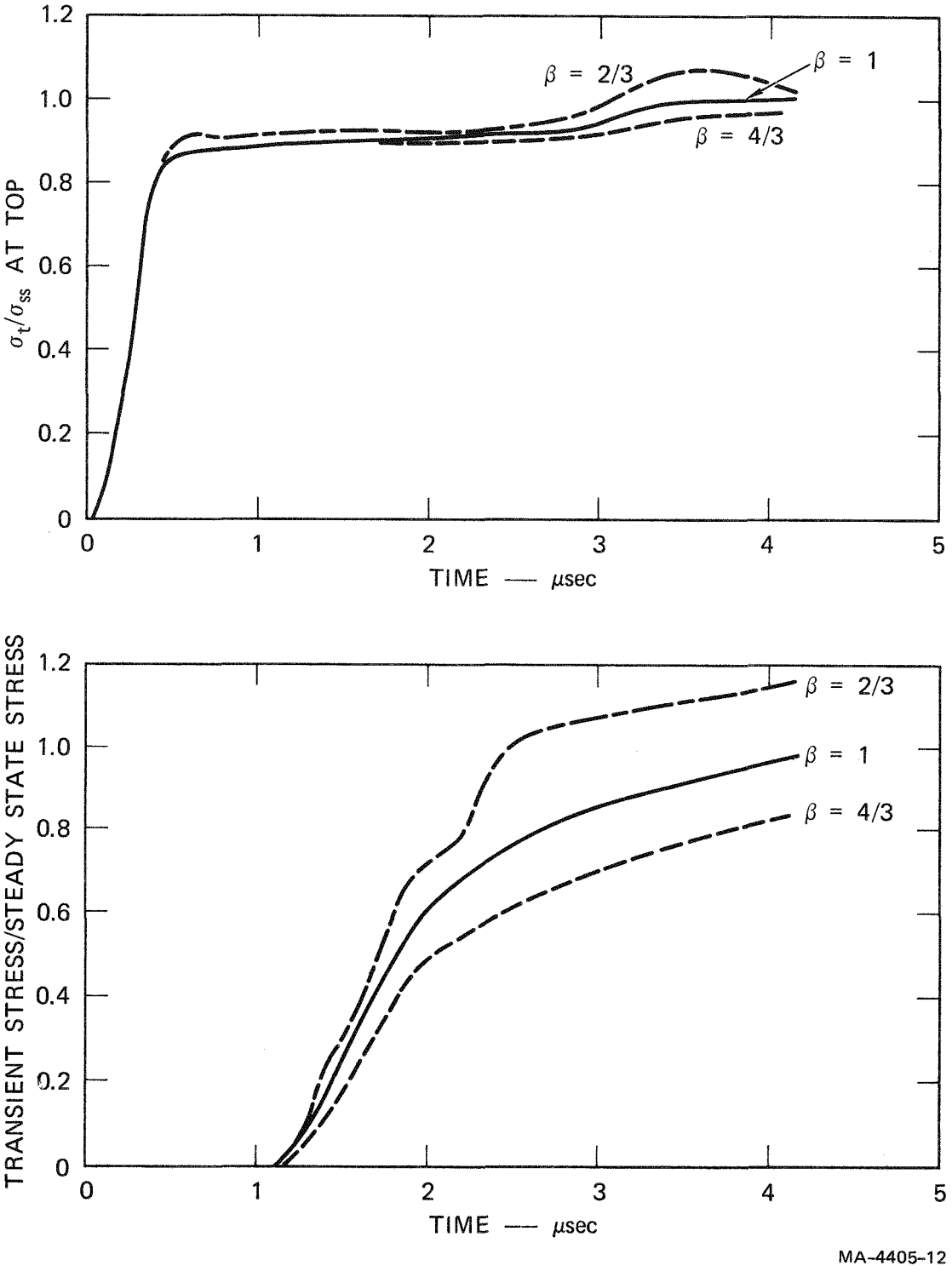

FIGURE B-1 EFFECT OF SEVERAL VALUES OF THE TIME CONSTANT β ON STRESS RELAXATION BEHAVIOR

For high values, the stress approaches 1.0 more slowly. The best relaxation parameter value appears to be $\beta = 1.0$. The stress near the bottom generally does not begin until after 1 μsec; then it rises rapidly to approach 1.0. As before, the optimum results are obtained for $\beta = 1.0$. An overshoot in stress may appear to occur for the uniform cell case for $\beta = 1.0$; however, the stress level was observed to be almost constant throughout the column. Thus, the calculation could be halted at 4.1 μs, the residual velocities set to zero, and an accurate static solution obtained. The results for the case in which a linearly varying velocity was initialized in the column suggest that somewhat faster convergence may be obtained with this feature. The velocity was arbitrarily selected and the choice may affect the suitability of the results.

Discussion

The preceding derivation has shown that adding a dynamic relaxation capability requires only the insertion of Equation (B-7) following the usual velocity calculation in wave propagation codes. Hence, almost no effort is required in the code modification.

The dynamic relaxation method described here is equivalent physically to attaching a velocity damping mechanism between each element and a fixed or static reference point. The damping quickly brings the material to a static equilibrium state. If a uniform velocity $\dot{U}_f$ were the desired end state, Equation (B-3) could be modified:

$$\frac{\partial^2 U_i}{\partial t^2} + \frac{2}{\tau}\left(\frac{\partial U_i}{\partial t} - \dot{U}_f\right) = \frac{\Sigma F_i}{M} \qquad \text{(B-11)}$$

Also, a different damping process could be included for each direction. For example, Equation (B-11) might be applied for radial velocities in a shell, while circumferential velocities would be undamped.

The computed results indicate that a dynamic relaxation coefficient of $\beta = 1.0$ is optimum when the time constant T is taken as the time for the elastic wave to travel once over the long direction of the sample. Smaller values of β/T induce unwanted oscillations, while larger values retard convergence. A faster convergence to the correct answer may be obtained by initializing a velocity distribution in the sample.

Appendix B

REFERENCES

1. J.R.H. Otter, Computations for Prestressed Concrete Reactor Pressure Vessels using Dynamic Relaxation, Nucl. Struct. Eng. 1965, Vol. 1, Amsterdam.

2. J.R.H. Otter, A. C. Cassell, and R. E. Hobbs, Dynamic Relaxation, Proceedings Instn. of Civil Eng., Paper 6986, January 1967.

3. D. J. Andrews and S. L. Hancock, A Relaxation Method for Solving Nonlinear Stress Equilibrium Problems, J. Comp. Physics, Vol. 12, No. 2, (June 1973).

4. S. L. Hancock, Numerical Convergence to Mechanical Equilibrium with a Velocity Damping Method and its Interpretation as Simultaneous Overrelaxation, TCAM Tech Memo 73-8, Physics International, San Leandro, California, July 1973.

Appendix C

INSERTION OF THE BFRACT SUBROUTINE INTO THE TOODY3 CODE

This appendix documents the changes required to incorporate the brittle fracture subroutine BFRACT[1] into TOODY3[2] or other two-dimensional wave propagation codes and describes the variables in the call statement.

The call to BFRACT is inserted just before the usual calculations for pressure and deviator stress. TXX, TYY, and TZZ are total stresses in orthogonal directions and are positive in compression (dyn/cm^2). NBFR is the number of cycles between prints from BFRACT.

```
      IF (NFR(M) · EQ·0) GØ TØ 2055
      IF (ENT(II,JJ) · NE · 0) GØ TØ 2052
C     CHECK THRESHØLD CRITERIØN
      IF (AMIN1(TXX,TYY,TZZ) ·GT · TSR(M,5)) GØ TØ 2055
C     CALL TØ BFRACT FØR STRESS CALCUIATIØNS
2052  CALL BFRACT(LS,DTZZ,DTXX,DTYY,DTXZ,EXX1,ETT1 EXY1 P3,ENM1,
     ENT1,VØ,VØLD,DT,E3,EEST,XFX01,XH01,XC01., TSR,XY01,YD,F,II,JJ,
     K3,NCYCLE,XRHØ01,DRØT,RØT1,FU1,CL,CN,IPRBFR,ENCR,ENEL,ENPL)
C     CALL TØ BFRACT FØR PRINTING
      IF(MØD(NCYCLE,NBFR) ·EQ·0) CALL BFRACT(2, etc...)
2055  CØNTINUE
```

---

1. L. Seaman and D. A. Shockey, Final Technical Report AMMRC CTR 72-2, Army Materials and Mechanics Research Center, Watertown, Massachusetts, 1975.
2. L. D. Bertholf and S. E. Benzley, Sandia Laboratory Research Report SC-RR-68-41, 1968.

The following describes the variables in the call statement. The column on the right gives the name of the variable as it is used inside the subroutine.

LS	indicator that causes BFRACT to initialize arrays = 0 initialize on this call = 1 computation only = 2 print only	LS
DTZZ	old deviator stress in the X direction, dyn/cm^2	SXXEN
DTXX	old deviator stress in the Y direction, dyn/cm^2	SYYEN
DTYY	old deviator stress in the theta direction, dyn/cm^2	STTEN
DTYZ	old shear stress, dyn/cm^2	TXYEN
EXX1	strain increment in the X direction	EXX1
EYY1	strain increment in the Y direction	EYY1
ETT1	strain increment in the T direction	ETT1
EXY1	shear strain increment (tensor basis)	EXY1
P3	pressure, dyn/cm^2	P
ENM1	relative volume of cracks	NM
ENT1	number of cracks ($number/cm^3$)	NT
VØ	new relative specific volume	VØ
VØLD	old relative specific volume	VØLD
DTØ	time step we entered with, second	DTØ
E3	old internal energy, erg/g	E
EEST	new estimated energy based on constant P through time step, erg/g	

XFK01	bulk modulus, dyn/cm^2	EQSTCM
XH01	Grüneisen ratio	EQSTGM
XG01	shear modulus, dyn/cm^2	ELMU
TSR	fracture parameters (array)	TSR
XY01	yield strength, dyn/cm^2	Y
YD	unused	YD
F	thermal strength reduction factor	F
	(range from 0 to 1.0)	
II	cell number in the K direction	KS
JJ	cell number in the J direction	JS
K3	material number	M
NCYCLE	cycle number	NN
RHØ01	original material density, g/cm^3	RHØS
DRØT	differential rotation (radians) positive	DRØT
	counterclockwise	
RØT1	cell rotation from beginning of fracture	RØT
FU1	fraction of unfragmented fractured material	FU2D
CL	cube of the crack radius (cm^3)	CL
CN	crack density (number/cm^3)	CN
IPRBFR	= 1 for extra BFRACT iteration printout	TPRBFR
ENCR	crack energy (erg/g)	ENCR
ENEL	elastic strain energy (erg/g)	ENEL
ENPL	plastic strain energy (erg/g)	ENPL

Of these variables, the ones newly introduced to TOODY3 for use in BFRACT or other fracture models are: NM,NT,TSR,DRØT,RØT,FU2D,CL,CN, IPRBFR,ENCR,ENEL,ENPL. Except for DRØT,TSR, and IPBFR, they are initialized in TOODY3 and arrays were set up in TOODY3 for storing their values cellwise as they are calculated. The TSR fracture parameters are read by TOODY3 when NFR = 2 and are listed here.

TSR PARAMETERS

TSR (1)	Growth constant = $3/4(4\eta)$, $cm^2/dyn/second$
TSR (2)	Growth threshold, dyn/cm^2
TSR (3)	Nucleation radius parameter, cm
TSR (4) and (6)	Parameters in the nucleation function number/cm^3/second and dyn/cm^2 $\dot{N}$ = TSR(4)*EXP(σ-TSR (5))/TSR(6)
TSR (5)	Nucleation threshold, dyn/cm^2
TSR (7)	Not used
TSR (8)	Threshold stress for entering BFRACT (usually equals TSR(5))
TSR (9)	Switch to indicate whether stress or deviator stress governs 0 stress
TSR (10)	Beta, ratio of number of fragments to number of cracks
TSR (11)	Gamma, ratio of fragment radius to crack radius
TSR (12)	Value of crack volume that defines threshold of coalescence
TSR (13)	TF, where fragment volume = $TF(RF)^3$

Appendix D

STRAIN RATE DEPENDENCE OF MICROFRACTURE ENERGY

Simple computations were performed to demonstrate the dependence of microfracturing energy on strain rate. We simulated microfracture nucleation and growth in a cube of Armco iron to which tensile stresses of equal magnitude were applied simultaneously in three perpendicular directions. Figure D-1 gives the results for three strain rates.

Figure D-1 shows that the external work goes initially into elastic energy as the cube sides are pulled apart. When the threshold stress for microcrack nucleation is reached, the fracturing process begins and energy starts to be absorbed. The rise in fracture energy occurs at the expense of the elastic strain energy, which begins to decrease. At higher strain rates, the elastic energy achieves higher values and the onset of fracture is delayed to higher strains. Most important, however, is that the energy absorbed in fracture increases enormously. The fracture energy in this case comprises the toughness, since plastic flow does not occur under triaxial stress conditions. Thus, for triaxial stress conditions or for brittle materials, the fracture toughness is strongly dependent on strain rate. In more plastic materials, the plastic work absorbed during crack propagation is much larger than the energy absorbed by microfracturing, and the rate dependence of the microfracture energy may have little consequence, except insofar as it determines when the

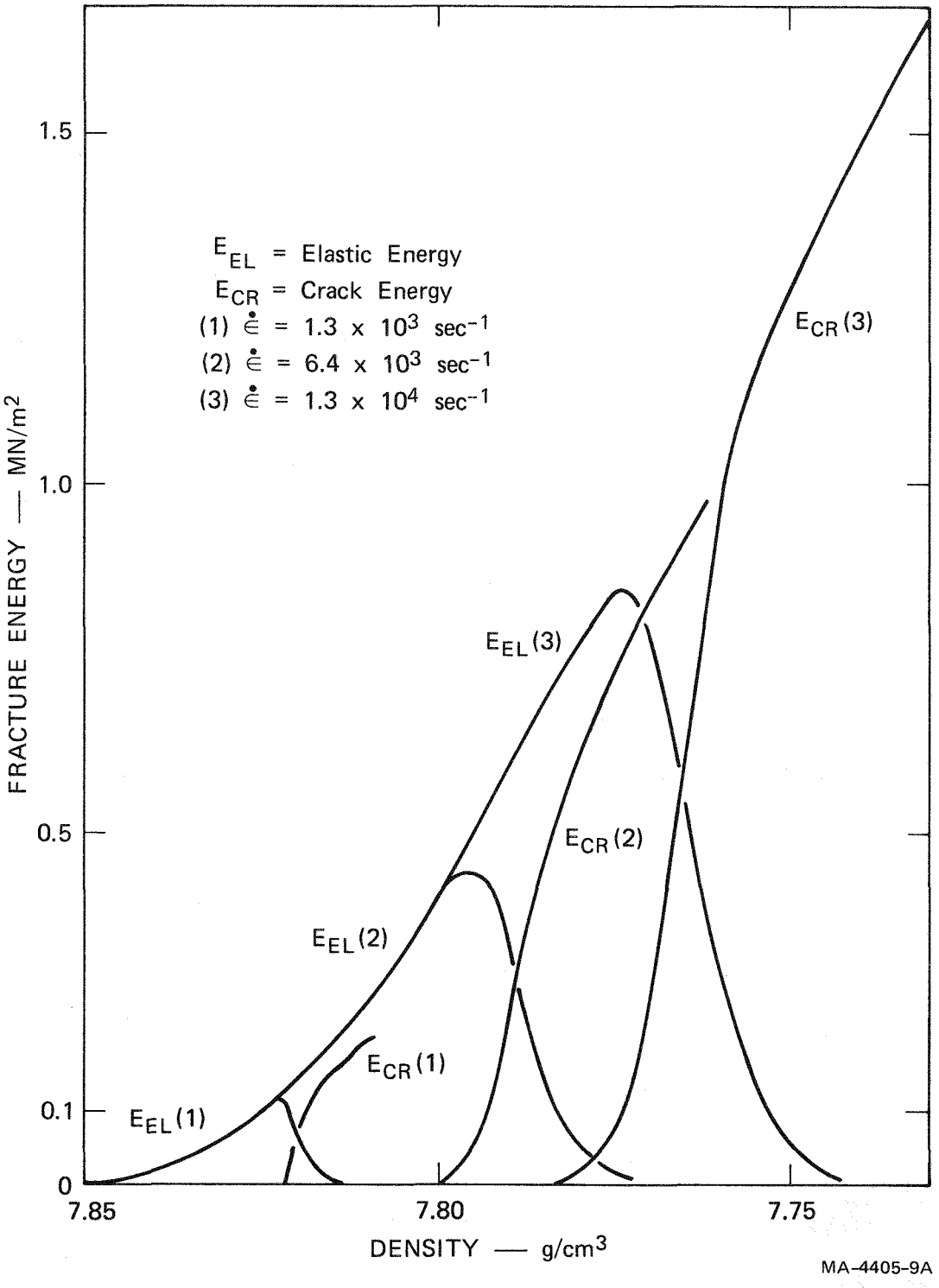

FIGURE D-1 STRAIN RATE DEPENDENCE OF THE FRACTURE ENERGY FOR ARMCO IRON

material element ruptures and the plastic work ceases. In such cases, the rate dependence of plastic deformation may be more important.